nature communications

Article

https://doi.org/10.1038/s41467-025-57646-4

Gradient all-nanostructured aerogel fibers for enhanced thermal insulation and mechanical properties

Received: 14 August 2024

Accepted: 25 February 2025

Published online: 10 March 2025

Check for updates

Xiaotong Fu[1,4], Lianmeng Si[2,4], Zhaoxin Zhang[3], Tingting Yang[1], Qichun Feng[1], Jianwei Song[2] ✉, Shuze Zhu[3] ✉ & Dongdong Ye[1] ✉

Lightweight, nanoporous aerogel fibers are crucial for personal thermal management and specialized heat protection. However, wet-spinning methods, exemplified by aramid aerogels, inevitably form a dense outer layer, significantly reducing the volume fraction of efficient thermal barrier nanovoids and limiting the development of ultimate thermal resistance in fibers. Herein, we develop a microfluidic spinning method to prepare gradient all-nanostructure aramid aerogel fibers (GAFs). Benefiting from the simultaneous shear alignment and diffusion dilution of a good solvent within the channels, the precursor gel fibers assemble into a structure with a sparse exterior and dense interior, which reverses during supercritical drying to form sheath and core layers with average pore diameters of 150 nm and 600 nm, respectively. Experiments and simulations reveal that the gradient nanostructure creates high interfacial thermal resistance at heat transfer interfaces, resulting in a radial thermal conductivity as low as 0.0228 W m^{-1} K^{-1}, far below that of air and wet-spun aerogel fibers. Moreover, GAF's unique nano-entangled network efficiently dissipates stress, achieving exceptionally high tensile strength (29.5 MPa) and fracture strain (39.2%). This work establishes a correlation between multiscale nanostructures and superlative performance, thereby expanding the scope of aerogel applications in intricate environments.

Thermal management systems within buildings and vehicles represent a substantial portion of global energy consumption, accounting for more than one-third of the total[1]. This significant energy expenditure notably contributes to CO_2 emissions, intensifying global carbon footprint[2,3]. Developing advanced insulation materials presents a viable solution to mitigate heat loss in various applications, including building walls[4], roofs, vehicle exteriors, and apparel[5], enhancing user comfort and curbing carbon emissions[6]. Actually, materials exhibiting high porosity (>0.9) are particularly effective in enhancing thermal insulation by limiting collisions between air molecules, elongating heat transfer pathways, and augmenting interface thermal resistance[7–9]. Distinguished by their abundant nanoporous structures, aerogels can be transformed into fibrous forms to preserve superior thermal insulation properties while attaining flexibility and fabricability, making them ideal for personal thermal management textiles. Currently, inorganic, polymeric, and composite aerogel fibers, including those made from silica, polyimide, cellulose, and hybrid materials, have shown promising insulation characteristics[10–13]. Nonetheless,

[1]School of Materials and Chemistry, Anhui Provincial Engineering Center for High-Performance Biobased Nylons, Anhui Engineering Research Center for Highly Functional Fiber Products for Automobiles, Anhui Agricultural University, Hefei, Anhui Province 230036, China. [2]State Key Laboratory for Strength and Vibration of Mechanical Structures, School of Aerospace Engineering, Xi'an Jiaotong University, Xi'an 710049, China. [3]Department of Engineering Mechanics, Institute of Applied Mechanics, Zhejiang University, Hangzhou 310000, China. [4]These authors contributed equally: Xiaotong Fu, Lianmeng Si.
✉e-mail: songjianwei@xjtu.edu.cn; shuzezhu@zju.edu.cn; ydd@whu.edu.cn

challenges remain, such as inadequate mechanical strength, limited thermal insulation performance, and elevated manufacturing costs, primarily due to the inconsistent control over micro- and nanoscale structures.

Aramid nanofibers (ANFs) are regarded as ideal nanostructured units due to their inherent high strength, environmental resilience, active sites, and excellent dispersibility, derived from polyphenylene terephthalate (PPTA)[14,15]. Aerogels assembled by ANFs exhibit outstanding thermal insulation properties to withstand extreme temperatures through three mechanisms: 1) reduced thermal conduction via the solid skeleton[16], 2) restricted thermal convection via the porous structure[17], and 3) multiple thermal radiation[18]. Currently, representative aerogel fiber manufacturing methods such as wet spinning[19], reactive spinning[20], and confined spinning[21], while enhancing scalability, inevitably reduce the precision of nanostructure control. This results in fibers exhibiting a dense skin layer on the exterior and a porous interior[22,23], along with a wide range of thermal conductivity (0.027–0.5 $W\,m^{-1}\,K^{-1}$)[24]. Previous researches indicate that the nanopore structure of aerogels significantly affects thermal conduction; transforming the dense packing structure of the shell layer into a loose nanostructure and optimizing the radial nanostructure distribution is expected to enhance the thermal insulation capabilities of aerogel fibers.

In this study, we unveil the development of gradient nanostructured aerogel fibers (GAFs), which exhibit exceptional thermal insulation properties, as corroborated by molecular simulations. Through the design of skin-core and gradient nanostructure models, we demonstrate that the outer-layer nanostructure of GAFs manifests a significantly superior thermal storage capacity and interfacial thermal resistance compared to skin-core aerogel fibers (SAFs), resulting in a 67% reduction in simulated thermal conductivity. Moreover, we have pioneered a manufacturing technique for producing GAFs using continuous microfluidic spinning technology. Coupled with supercritical drying, we have successfully fabricated aramid nanofiber aerogel fibers by precisely controlling solvent shear, diffusion, and sol-gel transition rates within the spinning channel. Compared to wet-spun aerogel fibers, GAFs exhibit increased porosity (from 98% to 98.6%), reduced density (from 20.5 kg/m^3 to 15.7 kg/m^3, enhanced tensile strength (from 10.9 MPa to 29.5 MPa), and significantly reduced thermal conductivity (from 0.0327 $W\,m^{-1}\,K^{-1}$ to 0.0228 $W\,m^{-1}\,K^{-1}$). Notably, the superior durability of aramid ensures stability under extreme cold, high temperatures, and vacuum conditions. The excellent comprehensive performance of GAFs significantly broadens their potential applications in textiles, construction, firefighting equipment, and even extreme aerospace scenarios, offering significant environmental benefits.

Results and discussion

The thermal insulation mechanisms of aerogel materials, encompassing multiple reflected radiation, reduced conduction, and restricted convection, are intricately linked to pore size and spatial distribution. Intriguingly, natural animal hair, exemplified by polar bears[25], and synthetic aerogel fibers, typically fabricated through wet spinning, exhibit dense outer layers, porous inner cores, and superior thermal insulation performance. To investigate the correlation between the nanostructure and thermal insulation, we employed coarse-grained molecular dynamics simulations under the same conditions to assess the radial heat transfer properties of two fibrous structural models with skin-core and gradient nanostructures (Fig. 1a; Supplementary Fig. S1). The results reveal that the two nanostructured fibers exhibit markedly different thermal distribution characteristics under the imposed flux from the heat source with temperature 2 (Lennard-Jones unit) to the heat sink with temperature 1 (Lennard-Jones unit). Unlike the skin-core fibers, whose dense outer layer nanostructure results in low interfacial thermal resistance, the gradient nanostructured fibers possess a loose nanoporous outer layer, which demonstrates high heat storage capacity and forms substantial interfacial thermal resistance at the gradient interface, thereby restricting radial heat transfer. Furthermore, quantitative simulations of the dimensionless thermal conductivity for both fiber types indicate a 40% reduction in thermal conductivity for the gradient nanostructured fibers compared to the skin-core fibers. These findings provide theoretical evidence that regulating aerogels' radial nanostructure size and spatial distribution can significantly enhance thermal insulation performance.

Guided by the simulation, we developed the gradient all-nanostructured aramid aerogel fibers (GAFs) from uniform aramid nanofibers (ANFs) dispersion (Supplementary Fig. S2) based on a spinning system integrated with nanoexfoliation, microfluidic spinning, sol-gel transition, and supercritical CO_2 drying process (Fig. 1b). Contrary to the skin-core aerogel fibers (SAFs) with dense shells and porous core configuration engendered by wet spinning (Fig. 1c), GAF is devoid of a dense exterior skin layer (Fig. 1d). ANF interweaves to forge a wholly nanoporous structure, congruent with the theoretical blueprint and rendering it an optimal candidate for thermal insulation. Additionally, the spinning system demonstrates the feasibility of large-scale fiber production (Fig. 1e, Supplementary Movie 1), which can be further woven into fabrics (Fig. 1f) owing to improved mechanical properties (discussed in detail later).

The formation of GAFs undergoes three key stages (Fig. 2a): 1) Heterogeneous spatial distribution of ANF induced by complex flow in a microfluidic chip: when the sheath flow of DMSO solvent is injected at an angle into the central channel containing ANF dispersion (DMSO/KOH), it not only enhances the shear orientation of ANF but also dilutes the ANF solution from the outside in, creating a concentration gradient with lower concentration at the exterior and higher concentration at the center due to shear orientation along the channel and diffusion dilution perpendicular to the channel; 2) Sol-gel transition induced by protonation: upon entering the acidic coagulation bath, the ANF undergoes protonation, rapidly triggering gelation and freezing the gradient structure, resulting in gel fibers with loose pores on the exterior and smaller pores on the interior (Supplementary Fig. S3); 3) Structural inversion during supercritical drying: During the solvent exchange process to form alcohol gel fibers, as the ethanol concentration in the solution increases, large pores on the fiber surface gradually collapse into smaller pores (Supplementary Figs. S4). Once the ethanol concentration exceeds 20%, all large pores with high surface porosity collapse into smaller pores (Supplementary Figs. S5), ultimately forming gradient all-nanostructured aerogel fibers after supercritical CO_2 drying (Fig. 2b).

We subsequently compared the structural assembly differences between SAFs produced by wet-spinning and GAFs constructed via microfluidic spinning (Fig. 2c). SAFs exhibited a nanoporous core (Fig. $2c_1$) and a distinct dense skin layer approximately 100 nm thick (Fig. $2c_2$, $2c_3$), as confirmed by cross-sectional SEM images. The GAFs core displays a similar nanoporous structure to SAFs (Fig. $2c_4$), with an average pore size of about 500 nm (Supplementary Fig. S6), while the outer layer maintains a nanoporous structure with an average pore size of 160 nm (Fig. $2c_5$; Supplementary Fig. S7) and shows a pronounced gradient interfacial layer (Fig. $2c_6$). Notably, altering the flow rate of DMSO from 500 to 1500 μL/min enables the regulation of the gradient nanoporous outer layer structure (from loose to dense) and thickness (from 20% to 60%), showcasing the excellent customizable structural capabilities of the microfluidic spinning system (Supplementary Fig. S8).

Furthermore, we characterized the variation in the intensity of the characteristic peak of the aramid I band (peak position at 1610 cm^{-1}) along the diameter of the aerogel fibers (Fig. $2d_1$), which visually illustrates the differences in ANF packing density between the two types of aerogel fibers. The results indicate that the Raman scattering intensity on the surface of SAFs is significantly higher than that within

the fiber (Fig. 2d$_2$), suggesting the presence of a highly compact thin layer on the surface. In contrast, GAFs show a uniformly decreasing scattering intensity from the exterior to the interior (Fig. 2d$_3$), indicating that the packing density outside the fiber is slightly higher than that inside, exhibiting a gradient transition. Raman imaging further confirms the distinct assembly structures of the two fiber types.

To elucidate the impact of nanostructures on the properties of aerogel fibers, we initially assessed the mechanical properties of SAFs and GAFs. The results indicate that SAFs with a dense skin layer exhibit a higher Young's modulus, reaching 112.74 MPa, a 37.7% increase over GAFs (81.9 MPa) (Fig. 3a; Supplementary Fig. S9). However, SAF's tensile strength (10.9 MPa), fracture strain (17.8%), and toughness (1.06 MJ m^{-3}) are significantly lower than those of GAFs (29.5 MPa, 39.2%, and 5.7 MJ m^{-3}), demonstrating the potential of gradient nanostructures in enhancing aerogel mechanical properties. Notably, GAFs developed in this work show superior mechanical properties compared to classical ANF-based fibers[26,27] and films[28] (Fig. 3b). As a performance demonstration, a single GAF can bear a weight of 50 g (Fig. 3c). After 1000 cycles of stretching to a strain of 0.5 mm, the mechanical properties of GAFs remain almost unchanged (Supplementary Fig. S10), and the morphology shows negligible alteration (Supplementary Fig. S11). To explore the deeper mechanisms of gradient nanostructure reinforcement and toughening, we employed molecular dynamics simulations to evaluate the deformation processes of SAFs and GAFs (Supplementary Fig. S12). The simulations revealed distinct fracture behaviors: as the simulated strain (ε) increased from 2 to 5, due to the small thickness of the dense nanofiber layer on the surface of SAFs, at microscopic large deformation, the dense layer can no longer maintain structure integrity, leading to micro-crack formation that exposes the internal nanostructure (Fig. 3d$_1$, Supplementary Movie 2); in contrast, GAFs maintained structural integrity during stretching, with outer nanopores aligning and deforming with the fiber, avoiding severe damage and retaining good mechanical properties (Fig. 3d$_1$, Supplementary Movie 3). The simulated stress-strain curves also reflected this trend (Fig. 3d$_2$).

Previous researches indicate that the specific functional group deformation under external force induces a redshift (Δν) in characteristic Raman peaks[29–31]. Thus, we employed Raman imaging to investigate the relationship between the Raman shifts of the amide I band $C=O$ stretching vibration in 5% deformed Kevlar fiber, SAFs, GAFs, and even isotropic ANF-assembled membrane (Supplementary Fig. S13), aiming to elucidate the correlation between nanostructure and internal stress during deformation. We first tested the Raman spectra of isotropic ANF-assembled membrane prepared by the vacuum filtration method, confirming that the characteristic Raman shift of $C=O$ in the relaxed state of PPTA molecular chains is

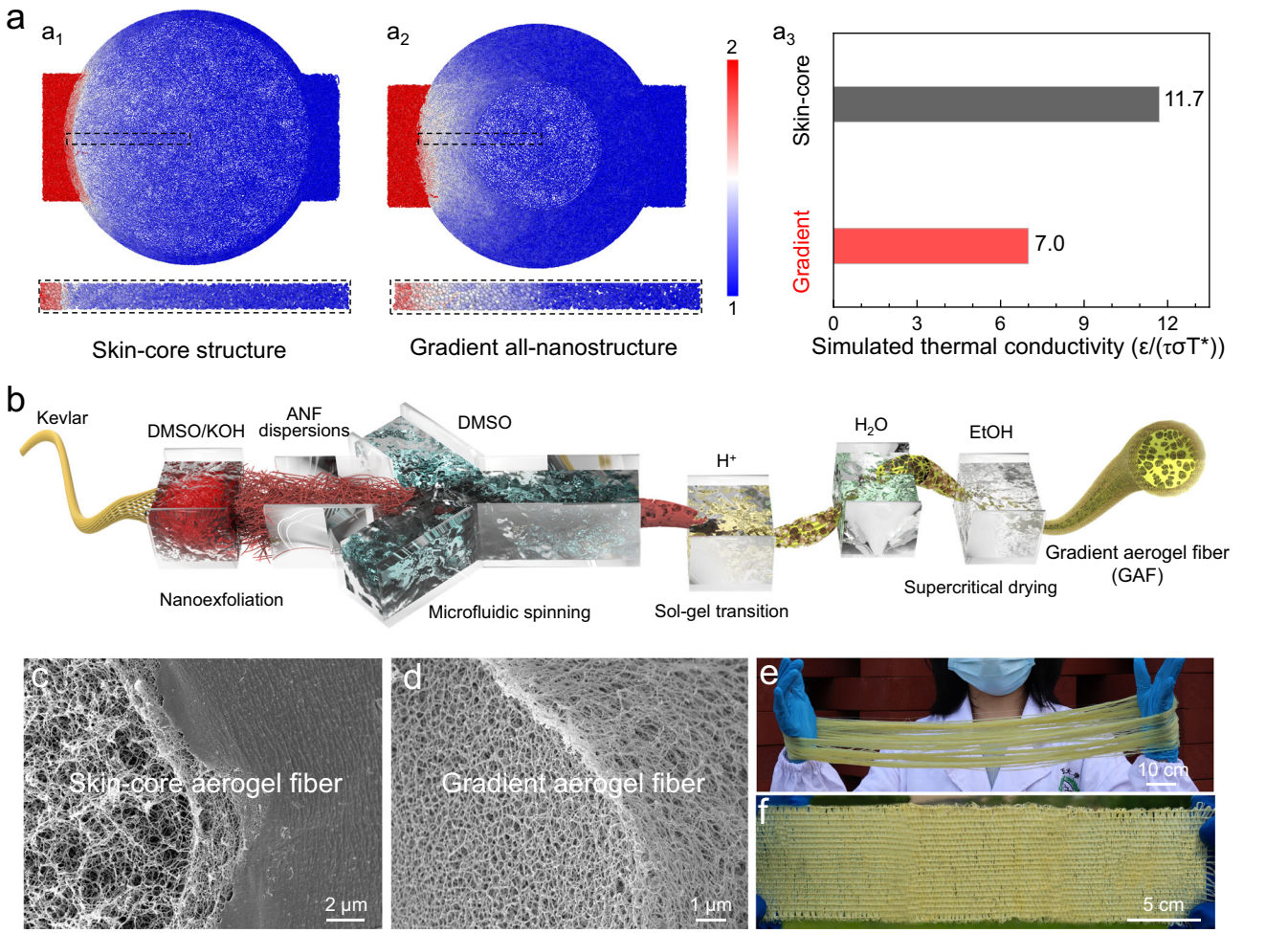

Fig. 1 | Thermal simulation and gradient nanostructured aerogel fibers (GAFs) preparation. a Coarse-Grained molecular dynamics simulations of thermal insulation for skin-core (**a$_1$**) and gradient nanostructured (**a$_2$**) models, with the radial temperature distribution map within the region marked by dashed box placed at the bottom and the simulated thermal conductivities (in Lennard-Jones unit) through the gradient interface of the gradient nanostructured model and the bulk of the skin-core model on the right (**a$_3$**). **b** Sketch map for the preparation of GAFs, including nanoexfoliation (ANF is the abbreviation for aramid nanofibers), microfluidic spinning, sol-gel translation, and supercritical drying. **c, d** Representative SEM images of skin-core and gradient nanostructured aerogel fibers. **e, f** Scalability of GAFs and textiles. Source data are provided as a Source Data file.

https://doi.org/10.1038/s41467-025-57646-4

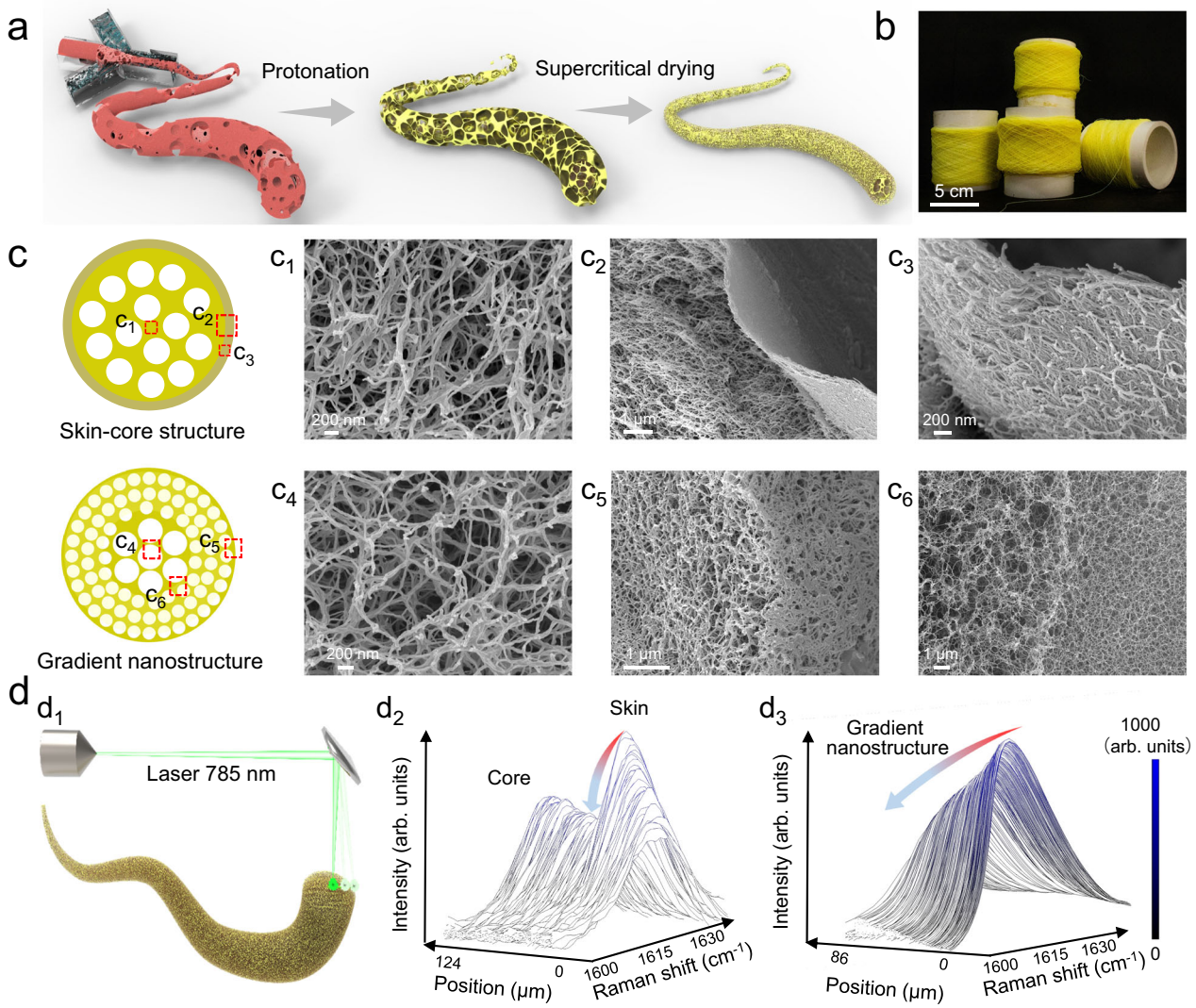

Fig. 2 | Forming mechanism and morphological characterization of GAFs. **a** Schematic illustration of nanostructure changes during GAFs preparation, including ANF dispersion in the microfluidic system, sol (red color)-gel (yellow color) transition in the coagulation bath, and ethanol solvent exchange. **b** Photograph of GAFs. **c** Cross-sectional SEM images of SAFs and GAFs at various locations during wet-spinning and microfluidic spinning, including center positions (**c_1**, **c_4**), edge positions (**c_2**, **c_3**, and **c_5**), and gradient interface position (**c_6**). **d** Schematic of Raman line imaging along the diameter (**d_1**), with representative Raman spectra selected at equal intervals from the exterior to the interior of SAFs (**d_2**) and GAF (**d_3**).

1656.5 cm^{-1} (Supplementary Fig. S13a). Comparing the 2D Raman imaging of the three types of fibers, we found that the Kevlar fiber mainly exhibits a low Raman shift in the red distribution (Fig. 3e_2; Supplementary Fig. S13b), with an average Δν of 5.6 cm^{-1} (Fig. 3e_5). In contrast, SAFs show significant stress concentration only in the densely packed skin layer (Fig. 3e_3; Supplementary Fig. S13c), with a Δν of 1.2 cm^{-1} (Fig. 3e_6), leading to initial high modulus and outer layer failure due to high internal stress during stretching. Interestingly, GAFs show the smallest overall Raman redshift (Fig. 3e_4; Supplementary Fig. S13d), with a Δν of only 0.3 cm^{-1} (Fig. 3e_7), indicating that the nanostructure effectively dissipates stress during stretching, resulting in the lowest internal stress and superior mechanical properties.

Subsequently, we evaluated the thermal insulation properties of skin-core and gradient-structured aerogel fibers and fabrics. Initially, we monitored the temperature changes atop a hot stage using an infrared thermal imager for both SAFs and GAFs specimens (Supplementary Fig. S14). The results indicated that when the hot stage was set at 200 °C, the top temperature of the GAF sample was only 190.3 °C, significantly lower than that of the SAF specimen (193.5 °C), demonstrating superior insulation capabilities. Further, we weaved the two aerogel fibers into fabrics and compared their thermal insulation properties under the same weight or thickness conditions (Fig. 4a). The findings revealed enhanced performance across various metrics (Fig. 4b, c). Additionally, we examined the thermal insulation properties of GAF fabrics of varying thicknesses across a broad temperature range (−30 °C to 270 °C) (Supplementary Figs. S15a, c). The results showed that a 0.5 mm GAF fabric could achieve temperature differentials of 33.4 °C and 63 °C at cold and heat templates, respectively (Supplementary Figs. S15b, d); when the fabric thickness increased to 1 mm, the insulation effect improved, yielding temperature differentials of 45.4 °C and 113 °C at cold and heat templates, respectively (Supplementary Figs. S15b, d). Notably, the insulation effect of GAFs based on a microfluidic system surpassed that of most previously reported thermal insulation fibers, including synthetic fibers[32,33] (e.g., PVC, PI, porous PI, PS, PET), natural fibers[7,33–36] (e.g., silk, wood, wool, cotton, cotton aerogel, TCNF), inorganic fibers[37–39] (e.g., glass, rock wool, ceramic, silicon), and ANF aerogels[26,27,40] (KNF fibers, KNF films, ANF films) (Fig. 4d).

To investigate the relationship between GAFs-enhanced thermal insulating performance and nanostructures, we established simplified models: a uniform density model and a gradient density model to examine the temperature field spatial distribution during heat transfer

https://doi.org/10.1038/s41467-025-57646-4

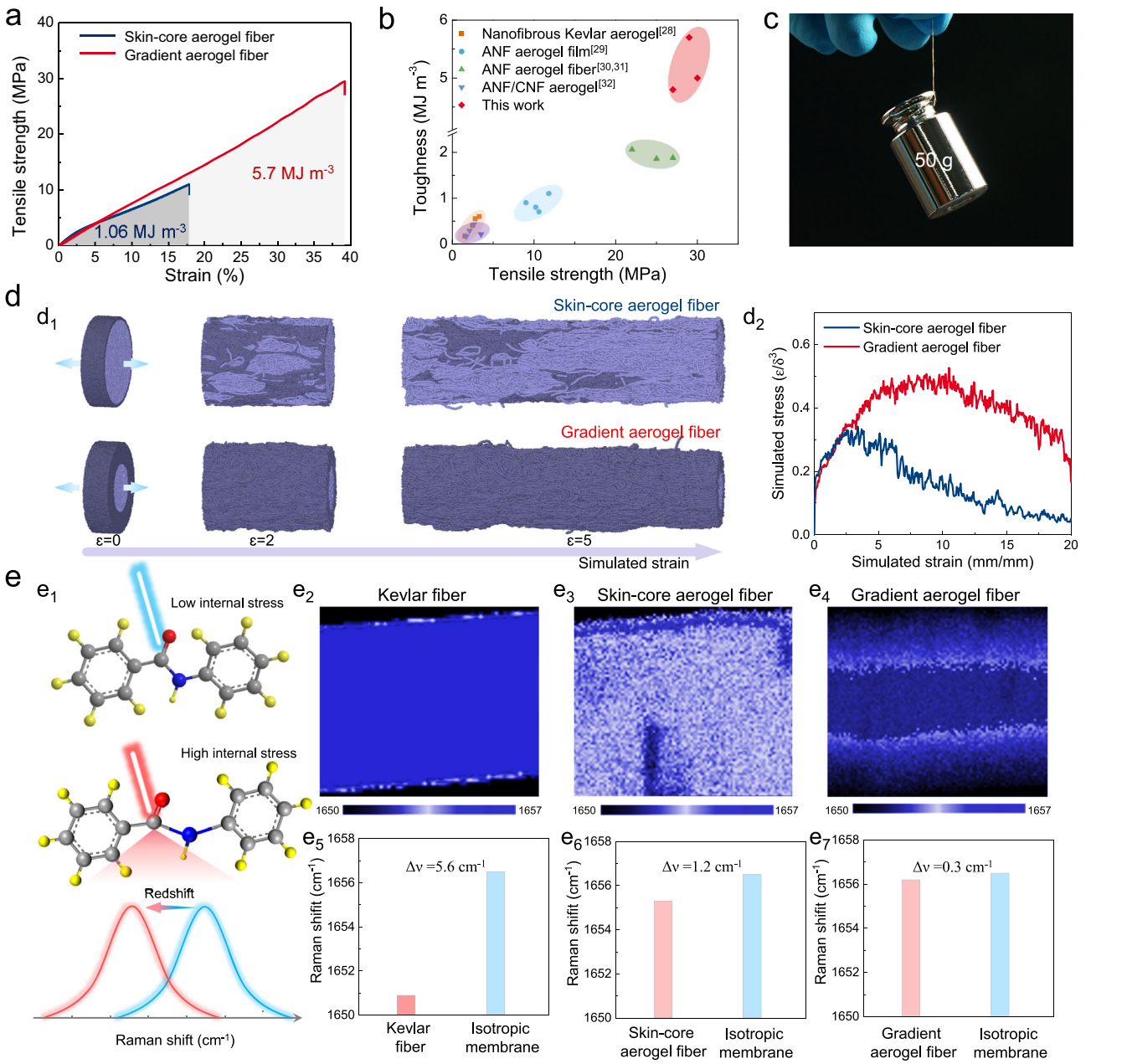

Fig. 3 | Study on the mechanical properties and deformation mechanisms of GAFs. a Stress-strain curves of SAFs and GAFs. **b** Comparison of toughness and tensile strength based on ANF aerogel materials[26–28,40,45]. **c** Photograph of a single GAF suspending a 50 g weight. **d** Simulation trajectories (**d_1**) and simulated stress-strain curves (**d_2**) for SAFs and GAFs models during tensile processes. **e** Raman imaging technique detecting internal stress levels in poly(p-phenylene terephthamide) based on characteristic Raman shift of *C* = *O* group, in the schematic, the yellow spheres represent hydrogen (H), gray spheres represent carbon (C), blue spheres represent nitrogen (N), and red spheres represent oxygen (O) (**e_1**) and the representative 2D Raman images and Raman shifts of Kevlar fiber (**e_2**, **e_5**), SAFs (**e_3**, **e_6**), and GAFs (**e_4**, **e_7**) under 5% tensile strain. Source data are provided as a Source Data file.

(Supplementary Fig. S16) at simulated time 10000τ. Under a simulated temperature gradient of 450 K (left) to 300 K (right), the uniform density model (representing SAFs) showed a smoothly varying temperature trend (Fig. 4e). Conversely, the gradient density model (representing GAFs) exhibited a noticeable temperature drop at the density interface (Fig. 4f), indicating greater thermal resistance at this interface. We calculated the energy accumulation of heat sources and sinks for both models. Figure 4g shows two models as a function of time. Due to the interface thermal resistance, less energy is transmitted in the gradient density model at a given time. Furthermore, the simulated thermal conductivity shows the contrast in energy supplied from heat sources and energy drained to heat sinks for the uniform density structure was 11.7 (Lennard-Jones unit, or 0.054 W m^{-1} K^{-1} in real unit). In contrast, the gradient density structure was 7.0 (Lennard-Jones unit, or 0.032 W m^{-1} K^{-1} in real unit), whose magnitudes and decreasing trend agree with experimental measurements (Fig. 4h). Additionally, we constructed high-density phase models with varying thicknesses to explore the effect of outer layer (microporous region) thickness on thermal barrier performance. Results show increased outer layer thickness improves thermal barrier effectiveness (Supplementary Figs. S17, S18, S19). Experimental findings further validate the computational conclusions (Supplementary Fig. S20). Both the computational insights and the experimental results confirm the feasibility and necessity of gradient nanostructures in enhancing thermal barrier performance.

In summary, we develop gradient all-nanostructure aramid aerogel fibers (GAFs) facilitated by microfluidics. The concurrent shear

https://doi.org/10.1038/s41467-025-57646-4

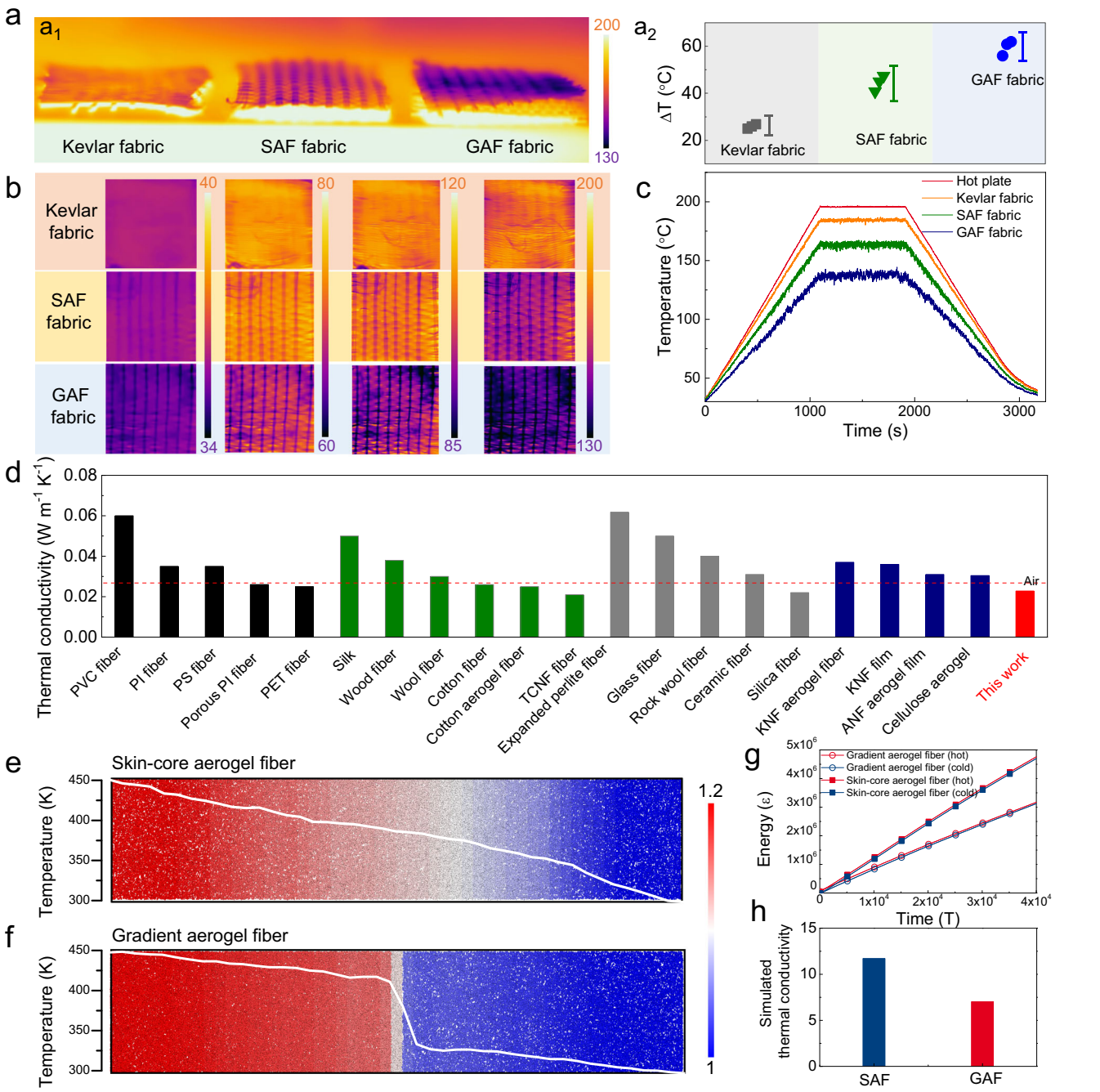

Fig. 4 | Investigation of thermal insulation properties and mechanism of gradient all-nanostructure aramid aerogel fibers (GAFs). a Heat plate experiment with equal-weight fabrics: Infrared thermal images of Kevlar, skin-core aerogel fibers (SAFs), and GAFs fabrics on a heat source ($\mathbf{a_1}$); Temperature drop between the heat plate and Kevlar, SAFs, and GAFs fabrics ($\mathbf{a_2}$), bars represent the range of ΔT. **b** Heat plate experiment with 0.5 mm thick fabrics: Kevlar, SAFs, and GAFs. **c** Temperature-heating time curves for Kevlar, SAFs, and GAFs fabrics on a heat source. **d** Comparison of thermal conductivity of GAFs with other natural and synthetic fibers[26,27,32–36,40]. **e** Simulated temperature profiles at t = 10000τ for a uniform density model under identical heat source and sink conditions. **f** Simulated temperature profiles at t = 10000τ for a gradient density model under identical heat source and sink conditions. **g** Energy-time curves at heat sources and sinks for uniform density and gradient density models during simulation. **h** Simulated thermal conductivities (in Lennard-Jones unit) of SAFs and GAFs. Source data are provided as a Source Data file.

alignment and solvent diffusion within the microfluidic channels enable the precursor gel fibers to form a structure characterized by a sparse outer layer and a dense inner core, which undergoes a reversal during supercritical drying, resulting in sheath and core layers with average pore diameters of 150 nm and 600 nm, respectively. Both experimental data and simulations indicate that this gradient nanostructure induces significant interfacial thermal resistance at heat transfer interfaces, leading to a remarkably low radial thermal conductivity of 0.0228 W m^{-1} K^{-1} for GAFs, significantly lower than that of air and wet-spun aerogel fibers. Additionally, the distinctive nano-entangled network within GAFs effectively dissipates stress, yielding extraordinary tensile strength (29.5 MPa) and fracture strain (39.2%). This research demonstrates a link between gradient nanostructures and exceptional mechanical and thermal performance, thereby broadening the potential applications of high-performance aerogels in construction, transportation, and specialized textiles.

Methods

Materials

Kevlar was purchased from Dupont Company. Dimethyl sulfoxide (DMSO), sodium hydroxide (NaOH), acetic acid, and Ethanol were all purchased from Aladdin Biochemical Technology Co., Ltd (Shanghai, China). The Millipore Milli-Q system prepared deionized water (3.8 μS/cm). All other chemicals were utilized without additional purification.

Preparation of ANF dispersion

The synthesis of ANF involved a deprotonation method[41]. The specific preparation process is as follows, Kevlar yarn (10 g) and KOH (15 g) were added to a mixture containing DMSO and water (500:25). The mixture was vigorously stirred for a week, resulting in a dark red dispersion of ANF.

Preparation of GAFs

A customized microfluidic chip with two phases and three channels, consisting of a core flow containing ANF solution and a sheath flow of DMSO, was utilized to produce gel fibril. The flow rates were meticulously regulated, with the core flow operating at 80 μL/min and the sheath flow ranging from 200 to 1200 μL/min, achieved by employing two flow pumps. The as-prepared gel fibril was wound onto a plastic roller at a constant speed of 25 rpm. It was then subjected to an extensive washing procedure using deionized water to remove residual DMSO, KOH, and acetic acid. The subsequent solvent exchange involved transferring the material into a blend of ethanol for 24 h and repeated three times. The GAFs were finally prepared by supercritical drying for 48 h.

Characterization

The morphology of GAFs and SAFs samples, coated with gold vapor, was characterized using a field emission scanning electron microscope (SIGMA 500, Zeiss, Germany) operated at an accelerating voltage of 5 kV. The pore size distribution in GAFs was quantified using Image J software. Raman spectroscopic analysis, including Raman spectra and spatial Raman imaging, was conducted using a Renishaw InVia Raman spectrometer equipped with a 532 nm laser. The concentration gradient of ANF was visualized through multivariate curve resolution facilitated by supplementary software. Mechanical properties of GAFs and SAFs were evaluated using a nanomechanical actuating transducer (NMAT) integrated into a Universal Testing Machine (Nano UTM T150, KLA-Tencor, USA) at a strain rate of 0.0027 s^{-1}. The fiber length in the test area is 10 mm, and the clamping method involves attaching the sample to a diamond-shaped paper frame using adhesive. Thermal insulation properties of the fabrics were assessed using a thermal infrared camera (InfReC R550, Avio, Japan) in an environment maintained at constant relative humidity (35%) and controlled specific temperatures, achieved via a heating stage (LINKAM, LTS420, UK). The camera captured thermal images at a frequency of one per second, monitoring temperature changes across the test area at a rate of 6 °C s^{-1}. Thermal conductivity was measured using a thermal conductivity analyzer (HS-DR-5, HESON Technology, China), employing a transient plane sensor with a 6.4 mm radius between two identical ANF aerogel fabrics. A compression device ensured optimal thermal contact between the sensor and the fabrics. The heating power was set at 20 mW, with each measurement lasting 10 s.

Coarse-grained molecular dynamics simulation

The effective thermal conductivity Λe of the thermal conduction region was calculated using the following formula:

$$q = \Lambda_e \frac{\Delta T}{\Delta L} = \frac{1}{2A}\left(\left|\frac{\Delta E_{Hot}}{\Delta t}\right| + \left|\frac{\Delta E_{Cold}}{\Delta t}\right|\right) \quad (1)$$

where q is the heat flux, A is the cross-sectional area perpendicular to the direction of heat conduction, Δt is the time step, E_{Source} and E_{Sink} are respectively the heat added to the source and subtracted from the sink, ΔL is the length of the thermal conduction region and ΔT is the temperature difference in that region.

We utilize coarse-grained molecular dynamics simulations to validate the impact of pores on the mechanical properties of aramid fibers. The coarse-grained bead-spring KG[42] model is employed in our simulations. Lennard-Jones units are used. Energy, length, and mass units are respectively set as ε, σ, and m. The pair-wise interaction forces between beads are represented by the Lennard-Jones potential:

$$E_{ij} = 4\varepsilon_{ij}\left[\left(\frac{\sigma_i}{r}\right)^{12} - \left(\frac{\sigma_i}{r}\right)^{6}\right] - 4\varepsilon_{ij}\left[\left(\frac{\sigma_i}{r_C}\right)^{12} - \left(\frac{\sigma_i}{r_C}\right)^{6}\right] r<r_C = 2.5 \quad (2)$$

Where r is the distance between two beads, $r_c = 2.5$ is the cutoff of interaction. ε_{ij} is the potential strength and σ_i is the size of the bead. For intrachain pair-wise interaction forces, $\varepsilon_{ij} = 1\varepsilon$ and $\sigma_i = 1\sigma$. For interchain pair-wise interaction forces, different ε_{inter} values are used to tune the density of fibers. Arithmetic mixing is used for pair-wise interaction between core and skin. All σ_i values are uniformly set to 1σ. The Unbreakable Finitely Extensible Nonlinear Elastic (FENE) potential is employed to describe the chemical bond interactions between particles.

$$U_{FENE}(r) = \_0.5KR_0^2 \ln\left[1 - \left(\frac{r}{R_0}\right)^2\right] \quad (3)$$

With $R_0 = 1.5\sigma$ is the maximum extent of the bond. K is the strength of bond interaction, $K = 30\varepsilon/\sigma^2$. The bond bending potential is harmonic style. $U_{angle} = \frac{K_\theta}{2}(\theta - \theta_0)^2$ with $K_\theta = 10\varepsilon$ per radian^2 is the strength of the interaction and $\theta_0 = 180°$ is the equilibrium bond angle. To scale the simulation units to real units, Set the LJ temperature unit $T^* = 1$ to correspond to the real unit of 300 K, so that $1\varepsilon = 4.14E^{-21}$ J. Set two consecutive beads to represent a $C_{14}H_{10}O_2N_2$ monomer (the chemical formula for each bead is C_7H_5ON), so that $1\sigma = 6.57E^{-10}$ m, and 1 m = 0.11912 kg/NA where NA is the Avagardonumber. The simulation time unit is $\tau = \sqrt{m\frac{\sigma^2}{\varepsilon}}$. The simulated thermal conductivity unit is $\varepsilon/(\tau\sigma T^*)$. All simulations are conducted using the LAMMPS[43] simulation package, and visualization is performed using the OVITO[44] software package. Model setup and simulation details for each model can be found in Supplementary Materials.

Data availability

The data supporting the findings of this study are available within the article and its Supplementary Information files and are available from the corresponding authors upon request. All data generated in this study are provided in the Supplementary Information. Source data are provided with this paper.

References

1. Zhong, X. et al. Global greenhouse gas emissions from residential and commercial building materials and mitigation strategies to 2060. *Nat. Commun.* **12**, 6126–6136 (2021).
2. Tian, X., Stranks, S. D. & You, F. Life cycle energy use and environmental implications of high-performance perovskite tandem solar cells. *Sci. Adv.* **6**, eabb0055 (2020).
3. Hill, C., Norton, A. & Dibdiakova, J. A comparison of the environmental impacts of different categories of insulation materials. *Energy Build.* **162**, 12–20 (2018).
4. Hua, S., Okello, M. O. & Zhang, J. Development of a vibration-damping, sound-insulating, and heat-insulating porous sphere foam system and its application in green buildings. *Sci. Rep.* **14**, 14277–14299 (2024).
5. Wu, R. et al. Spectrally engineered textile for radiative cooling against urban heat islands. *Science* **384**, 1203–1212 (2024).

6. Li, Z. et al. Solution-shearing of dielectric polymer with high thermal conductivity and electric insulation. *Sci. Adv.* **7**, eabi7410 (2021).
7. Zhao, X. et al. A scalable high-porosity wood for sound absorption and thermal insulation. *Nat. Sustain.* **6**, 306–315 (2023).
8. Liu, H. & Zhao, X. P. Thermal conductivity analysis of high porosity structures with open and closed pores. *Int. J. Heat Mass Transfer.* **183**, 122089 (2022).
9. Zhao, X. P., Brozena, A. H. & Hu, L. B. Critical roles of pores and moisture in sustainable nanocellulose-based super-thermal insulators. *Matter* **4**, 769–772 (2021).
10. Ahankari, S., Paliwal, P., Subhedar, A. & Kargarzadeh, H. Recent developments in nanocellulose-based aerogels in thermal applications: a review. *ACS Nano* **15**, 3849–3874 (2021).
11. Tafreshi, O. A. et al. A review on multifunctional aerogel fibers: processing, fabrication, functionalization, and applications. *Mater. Today Chem.* **23**, 100736 (2022).
12. Liu, Q. et al. Recent advances in novel aerogels through the hybrid aggregation of inorganic nanomaterials and polymeric fibers for thermal insulation. *Aggregate* **2**, e30 (2021).
13. Li, C. et al. Silica aerogels: from materials research to industrial applications. *Int. Mater. Rev.* **68**, 862–900 (2023).
14. Yang, B. et al. Fabrication, applications, and prospects of aramid nanofiber. *Adv. Funct. Mater.* **30**, 2000186 (2020).
15. He, H. et al. Ultrastrong and multifunctional aerogels with hyperconnective network of composite polymeric nanofibers. *Nat. Commun.* **13**, 4242–4250 (2022).
16. Zhao, H. Y. et al. Bioinspired intelligent solar-responsive thermally conductive pyramidal phase change composites with radially oriented layered structures toward efficient solar–thermal–electric energy conversion. *Adv. Funct. Mater.* **33**, 2302527 (2023).
17. Guo, Y., Ruan, K. & Gu, J. Controllable thermal conductivity in composites by constructing thermal conduction networks. *Mater. Today Phys.* **20**, 100449 (2021).
18. Shoaib, M. et al. Numerical investigation for rotating flow of MHD hybrid nanofluid with thermal radiation over a stretching sheet. *Sci. Rep.* **10**, 18533–18447 (2020).
19. Tang, Y., Chen, W. & Zhu, P. Towards superior thermal insulation: Flexible Kevlar aerogel fibers with ultrafine size. *Mater. Today Sustain.* **27**, 100902 (2024).
20. Wei, P. et al. Reactive spinning to achieve nanocomposite gel fibers: from monomer to fiber dynamically with enhanced anisotropy. *Mater. Horiz.* **7**, 811–819 (2020).
21. Hu, P. et al. Robust and flame-retardant zylon aerogel fibers for wearable thermal insulation and sensing in harsh environment. *Adv. Mater.* **36**, e2310023 (2024).
22. Sheng, Z. et al. The rising aerogel fibers: status, challenges, and opportunities. *Adv. Sci.* **10**, e2205762 (2023).
23. Bao, Y., Lyu, J., Liu, Z., Ding, Y. & Zhang, X. Bending stiffness-directed fabricating of Kevlar aerogel-confined organic phase-change fibers. *ACS Nano* **15**, 15180–15190 (2021).
24. Li, M. et al. Facile preparation of continuous and porous polyimide aerogel fibers for multifunctional applications. *ACS Appl. Mater. Interfaces.* **13**, 10416–10427 (2021).
25. Sheng, Z. & Zhang, X. Mimicking polar bear hairs in aerogel fibers. *Science* **382**, 1358–1359 (2023).
26. Li, J. et al. Highly compressible, heat-insulating and self-extinguishing cellulose nanofiber/aramid nanofiber nanocomposite foams. *Carbohydr. Polym.* **261**, 117837 (2021).
27. Li, L. et al. Folk arts-inspired twice-coagulated configuration-editable tough aerogels enabled by transformable gel precursors. *Nat. Commun.* **14**, 8450–8461 (2023).
28. Yang, S., Xie, C., Qiu, T., Tuo, X. The aramid-coating-on-aramid strategy toward strong, tough, and foldable polymer aerogel films. *ACS Nano*, **16**, 14334–14343 (2022).
29. Fu, X. et al. Aesthetic cellulose filaments with water-triggered switchable internal stress and customizable polarized iridescence toward green fashion innovation. *ACS Nano* **18**, 7496–7503 (2024).
30. Andrews, M. C. & Young, R. J. Analysis of the deformation of aramid fibres and composites using Raman spectroscopy. *J. Raman Spectrosc.* **24**, 539–544 (1993).
31. Lin, Z. Y. & Dongdong. Research progress in structural design of biomass materials aided by Raman imaging technology based on spectral information. *Basic Sci. J. Textile Univ.* **37**, 1–10 (2024).
32. Dos Santos, W. N., de Sousa, J. A. & Gregorio, R. Thermal conductivity behaviour of polymers around glass transition and crystalline melting temperatures. *Polymer Testing* **32**, 987–994 (2013).
33. Xue, T. et al. Polyimide aerogel fibers with controllable porous microstructure for super-thermal insulation under extreme environments. *Adv. Fiber Mater.* **4**, 1118–1128 (2022).
34. Jiang, Y. et al. Contrasting soil thermal responses to fire in Alaskan tundra and boreal forest. *J. Geophys. Res.: Earth Surf.* **120**, 363–378 (2015).
35. Xue, Y., Lofland, S. & Hu, X. Thermal conductivity of protein-based materials: A Review. *Polymers* **11**, 456–464 (2019).
36. Tong, T. et al. Thermal conductivity of single silk fibroin fibers measured from the 3ω method. *Int. J. Therm. Sci.* **185**, 108057 (2023).
37. Kono, J., Goto, Y., Ostermeyer, Y., Frischknecht, R. & Wallbaum, H. Factors for eco-efficiency improvement of thermal insulation materials. *Key Eng. Mater.* **678**, 1–13 (2016).
38. Uma, S., McConnell, A. D., Asheghi, M., Kurabayashi, K. & Goodson, K. E. Conduction and radiation in thermal analysis. *Int. J. Thermophys.* **22**, 605–616 (2001).
39. Shintani, Y., Nagaoka, T., Deguchi, Y., Ido, K. & Harada, K. Simple method to predict downward heat flux from flame to floor. *Fire Sci. Technol.* **33**, 17–34 (2014).
40. Hu, Y. et al. Proton donor-regulated mechanically robust aramid nanofiber aerogel membranes for high-temperature thermal insulation. *ACS Nano* **16**, 5984–5993 (2022).
41. Si, L. et al. A superstable, flexible, and scalable nanofluidic ion regulation composite membrane. *Sci. Bull.* **68**, 2344–2353 (2023).
42. Kremer, K. & Grest, G. S. Erratum: Dynamics of entangled polymer melts: A molecular-dynamics simulation. *J. Chem. Phys* **94**, 4103 (1991).
43. Thompson, A. P. et al. LAMMPS - a flexible simulation tool for particle-based materials modeling at the atomic, meso, and continuum scales. *Comput. Phys. Commun.* **271**, 108171 (2022).
44. Stukowski, A. Visualization and analysis of atomistic simulation data with OVITO–the Open Visualization Tool. *Modelling Simul. Mater. Sci. Eng.* **18**, 015012 (2010).
45. Lyu, J., Sheng, Z., Xu, Y., Liu, C. & Zhang, X. Nanoporous Kevlar aerogel confined phase change fluids enable super-flexible thermal diodes. *Adv. Funct. Mater.* **32**, 2200137 (2022).

Acknowledgements

This study was supported by the National Natural Science Foundation of China (Grant numbers. 52473090, 52103124, 12322205, 12002304), the Excellent Youth Scientists Fund from the Natural Science Foundation of Anhui Provincial Project (2408085Y025), and the Distinguished Young Scientists Fund from the Natural Science Foundation of Zhejiang Province (Grant number. LR23A020001).

Author contributions

D.Y. conceived the concept. D.Y., S.Z. and J.S. provided guidance and support throughout the project. X.F. took lead roles in performing the experiments, analyzing data, and drafting the manuscript. L.S. contributed to the preparation of ANF solution. T.Y. contributed to mechanical experimental tests. Q.F. contributed to thermal insulation experimental tests. Z.Z. and S.Z. contributed to computational

modeling. All authors contributed intellectually to the study design and approach, discussed the results, and reviewed and edited the final manuscript.

Competing interests
The authors declare no competing interests.

Additional information
Supplementary information The online version contains supplementary material available at https://doi.org/10.1038/s41467-025-57646-4.

Correspondence and requests for materials should be addressed to Jianwei Song, Shuze Zhu or Dongdong Ye.

Peer review information *Nature Communications* thanks the anonymous reviewer(s) for their contribution to the peer review of this work. A peer review file is available.